ARTICLE

Check for updates

Microwave-to-optical conversion in a room-temperature ^{87}Rb vapor for frequency-division multiplexing control

Benjamin D. Smith [1✉], Bahar Babaei [1], Andal Narayanan[1,2] & Lindsay J. LeBlanc [1✉]

Coherent microwave-to-optical conversion is crucial for transferring quantum information generated in the microwave domain to optical frequencies, where propagation losses can be minimized. Coherent, atom-based transducers have shown rapid progress in recent years. This paper reports an experimental demonstration of coherent microwave-to-optical conversion that maps a microwave signal to a large, tunable 550(30) MHz range of optical frequencies using room-temperature ^{87}Rb atoms. The inhomogeneous Doppler broadening of the atomic vapor advantageously supports the tunability of an input microwave channel to any optical frequency channel within the Doppler width, along with the simultaneous conversion of a multi-channel input microwave field to corresponding optical channels. In addition, we demonstrate phase-correlated amplitude control of select channels, providing an analog to a frequency domain beam splitter across five orders of magnitude in frequency. With these capabilities, neutral atomic systems may also be effective quantum processors for quantum information encoded in frequency-bin qubits.

[1] Department of Physics, University of Alberta, Edmonton, Alberta T6G 2E1, Canada. [2] Raman Research Institute, Bangalore 560080, India.
✉email: bdsmith@ualberta.ca; lindsay.leblanc@ualberta.ca

Quantum information processing using solid-state qubits, such as superconducting qubits or spins associated with defects in solid state systems, has shown rapid progress in the field of quantum information technology[1,2]. The typical operation frequency of these devices is ~10 GHz, in the microwave region of the electromagnetic spectrum. Due to the inherent room-temperature thermal-photon occupation of cables at GHz frequencies that leads to signal noise, practical implementation of scalable and distributed quantum networks at these frequencies poses a formidable challenge[3]. In recent years, progress has been made in addressing coherent conversion of signals from the microwave to optical regimes[4,5]: at optical frequencies, not only are the thermal noise photons negligible at room temperature, but there exist efficient single-photon detectors and technologies for quantum state storage and reconstruction.

Several systems have been used to coherently convert signals at microwave frequencies to the optical regime. These include electro- and magneto-optical devices[6,7], opto-mechanical structures,[8] and atoms with suitable internal energy level spacings[9–12]. Impressive progress on improving the efficiency of the conversion process led to efficiency near 80%[11], and the largest reported conversion bandwidths of an input microwave signal are 15–16 MHz[12–14]. Along with conversion bandwidth, a transducer that can accommodate several channels of input and output frequencies is advantageous, and tunability over input microwave frequencies across 3 GHz width was recently reported[15]. Yet, transducers that operate over multiple optical output frequencies have not been demonstrated to date.

In this article we show that a limited bandwidth input microwave signal can be converted to a large tunable range of output optical frequencies, across 550(30) MHz. This capacity enables information encoded in a narrow-bandwidth microwave field to be mapped to several frequencies in the optical domain, achieving coherent frequency-division multiplexing (FDM). The ability to tune the optical signal output over such a large frequency range arises because of the presence of a large inhomogeneous optical Doppler width for Rb atoms at room temperature. The Doppler width also enables an input multiple-channel microwave idler to be simultaneously and coherently converted to a multiple-channel optical-signal output. In addition, we demonstrate correlated amplitude control of the converted multi-channel optical field with the ability to selectively extinguish a desired output frequency channel. This action is very similar to the frequency domain beam-splitting operation for frequency bins, demonstrated using electro-optic modulators (EOMs) and pulse shapers[16].

Results

Coherent frequency-division multiplexing enables qubits encoded in a microwave frequency to be placed in any desired output optical channel within the range of tunability. Multiple qubits in different input microwave channels can also be coherently mapped to the optical domain. The ability to control the amplitude of selected output optical channels is very useful in performing single-qubit-gate operations spanning involving both microwave and optical frequencies. With a channel linewidth of about 30 Hz, this results in a large channel capacity of about 10^7 channels over the output tunable range. Thus neutral atom systems are a promising candidate as a quantum frequency processor platform[17] for quantum information encoded in frequency bin qubits.

Numerical model

Microwave-to-optical conversion in a room-temperature ^{87}Rb atomic vapor is possible through a sum-frequency generation (SFG) process analogous to a RF mixer

[Fig. 1a] and depicted in Fig. 1c. The nonlinear process uses a hybrid, magneto-optical second-order [$\chi^{(2)}$] susceptibility induced in the vapor by the interaction of three energy levels with an optical pump (electric-dipole transition) and a microwave idler (magnetic-dipole transition) fields. (Note that isotropic atomic systems with only electric-dipole transitions have a $\chi^{(2)}$ of zero.) The idler field (ω_I) is supported by the TE$_{011}$ mode of a cylindrical copper microwave cavity[18,19] [Fig. 1b] and connects the $|b\rangle \equiv |5S_{1/2}, F = 1\rangle$ and $|c\rangle \equiv |5S_{1/2}, F = 2\rangle$ ground state levels. The pump frequency ω_P is, chosen anywhere within the Doppler width [Fig. 1c], and connects the $|c\rangle$ and $|a\rangle \equiv |5P_{3/2}, F' = 1, 2\rangle$ levels. We define δ as the detuning of the pump field from the the mid-energy point between the $|F' = 1\rangle$ and $|F' = 2\rangle$ excited levels. In SFG, the pump combines coherently with the idler to generate a new optical signal field at frequency $\omega_S = \omega_P + \omega_I$.

We begin by establishing a numerical model that explains the large frequency tunability and multi-channel conversion capability observed in this experiment, similar to that discussed for a generic, three-level, room-temperature atomic system, with interacting idler, pump, and signal fields[20]. The Rabi frequencies of the idler and pump fields at position z are $\Omega_I(z) = \boldsymbol{\mu}_{cb} \cdot \mathbf{B}_I(z)$ and $\Omega_P(z) = \mathbf{d}_{ac} \cdot \mathbf{E}_P(z)$, where $\Delta\varphi$ is the relative phase between the fields, and $\boldsymbol{\mu}_{cb}$ and $\mathbf{d}_{ac}$ are the dipole matrix elements between $|c\rangle$ & $|b\rangle$ and $|a\rangle$ & $|c\rangle$ levels. The signal field is generated due to a sum-frequency interaction between the idler and pump fields. The Rabi frequency of the generated signal field $\Omega_S(\ell)$ after a medium of length ℓ, under a rotating wave and three-photon transformation, is (see Supplementary Note 4)

$$\Omega_S(\ell) = \frac{i\Omega_P(0)\Omega_I(0)e^{-i\Delta\varphi}}{2\Gamma_2}(e^{-\beta\ell} - 1), \tag{1}$$

where the constant

$$\beta = \frac{2\eta_S\Gamma_2\Gamma_3}{4\Gamma_1\Gamma_2\Gamma_3 + \Gamma_3|\Omega_P(0)|^2 + \Gamma_2|\Omega_I(0)|^2}, \tag{2}$$

and

$$
\begin{aligned}
\Gamma_1 &= \frac{\gamma_P}{2} + \frac{\gamma_S}{2} - i\Delta_S(\boldsymbol{\nu}), \\
\Gamma_2 &= \frac{1}{2}\gamma_I - i[\Delta_S(\boldsymbol{\nu}) - \Delta_P(\boldsymbol{\nu})], \\
\Gamma_3 &= \frac{\gamma_P}{2} + \frac{\gamma_S}{2} + \frac{\gamma_I}{2} - i\Delta_P(\boldsymbol{\nu}), \\
\eta_S(\nu) &= \boldsymbol{d}_{ac}^2\omega_s N(\nu)/2\epsilon_0 c,
\end{aligned}
\tag{3}
$$

with $N(\nu)$ is the number density of atoms in the velocity class with $\nu = |\boldsymbol{\nu}|$. The value $N(\nu)$ is the Maxwell-Boltzmann (MB) velocity distribution of atoms at room temperature. The Doppler-shifted detunings of the pump and the generated signal fields, as seen from the atom frame [Fig. (2a, iii–v)], are denoted as $\Delta_P = \delta_P - \boldsymbol{k}_P \cdot \boldsymbol{v}$ and $\Delta_S = \delta_S - \boldsymbol{k}_S \cdot \boldsymbol{v}$, while the corresponding detunings in the lab frame are δ_P & δ_S [Figs. 1c and 2a, i]. The microwave idler field has negligible Doppler shift for all velocity values. The natural decay rates from the $|a\rangle$ level to both the $|c\rangle$ and $|b\rangle$ levels are denoted by γ_P and γ_S, respectively [Fig. 1c].

To maximize the generated signal field, sufficiently high input pump and idler field intensities and a small value for Γ_2 [Eq. (1)] are required. From Eq. (3) this is achieved when

$$\Delta_S(\boldsymbol{\nu}) - \Delta_P(\boldsymbol{\nu}) = 0. \tag{4}$$

Typically, the wavelengths of optical fields are such that $k \equiv |\mathbf{k}_S| \approx |\mathbf{k}_P| \gg |\mathbf{k}_I|$, in which case Eq. (4) reduces to $(\delta_S - \delta_P) = 0$. Since the signal and pump fields travel in the same direction, the phase-matching condition $\mathbf{k}_I + \mathbf{k}_P = \mathbf{k}_S$ is automatically satisfied for all atomic velocity classes.
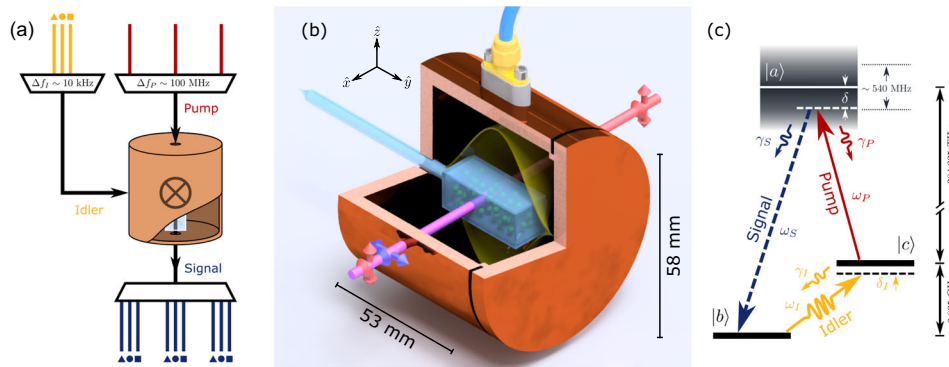
Fig. 1 Main components of the experiment. a Schematic of the atomic frequency-division multiplexing scheme. The microwave cavity-vapor cell system acts analogously to an RF mixer, and information encoded in idler (yellow) channels (▲, ●, ■) is combined coherently with multiple pump (red) channels to produce many output signal (blue) channels over a range of optical frequencies. **b** A representation of our microwave cavity and the generation process. The optical pump beam passes transversely through the cavity and cell and is polarized along the z-axis, parallel to a weak magnetic field. The cavity's TE_{011} mode overlaps with the pump interaction region inside the vapor cell. The arrows define the beam propagation and polarization directions. **c** Three-level energy diagram showing the cyclical transition scheme. The idler (ω_I) and pump (ω_P) fields combine coherently in the vapor to produce the signal field (ω_S). The frequencies shown are for ^{87}Rb; in a room-temperature vapor, the excited state addressed by the pump field is Doppler-broadened by ~550 MHz.

The maximum signal generation for each velocity class is obtained when δ_S of the signal-field is the same as the pump-field detuning δ_P, such that different velocity classes participate in the maximum signal-field generation at different pump-field detunings. Therefore, changing the laboratory pump frequency within the Doppler width to $\omega'_P = \omega_P + \delta$ gives rise to a corresponding signal field at $\omega'_S = \omega_S + \delta$, thus enabling a large tunable generation bandwidth. This is depicted numerically in Fig. 2a, ii for atoms at $T = 300$ °C. The shape of the generated signal field is primarily determined by the MB velocity distribution.

The broad Doppler width at room temperature and guaranteed phase-matching for sum-frequency generation [Eq. (4)] make possible the simultaneous conversion of multi-channel microwave field inputs to a multi-channel optical signal outputs [Fig. 2b]. Multiple frequency channels in the idler and pump fields are obtained by either amplitude or phase modulation. Specifically, the idler field amplitude is modulated as $\Omega_I(t) = \Omega_{I0}(1 + a_m \sin(\omega_{AM})t)$ and phase modulation of the pump field takes the form $\Omega_P(t) = \Omega_{P0} \sin(\omega_P t + p_m \sin(\omega_{PM})t + \Delta\phi)$. The symbols a_m and p_m denote amplitude and phase modulation indices. The modulation frequencies are ω_{AM} and ω_{PM} and $\Delta\phi$ denotes the relative phase between the two modulation fields. By multiplying the modulated idler and pump fields to obtain the signal field, we derive the amplitudes for the generated signal field and its first-order side-bands for the case of equal modulation frequencies $\omega_{AM} = \omega_{PM} = \delta$ and for equal modulation indices $a_p = a_m = 0.2$. At equal modulation frequencies, the pump and idler fields associated with the sideband channels interfere with each other [Fig. 2c] enabling control of their amplitudes through $\Delta\phi$[21]. The powers of the positive and negative sideband channels at $\omega_S \pm \delta$ are proportional to $a_m^2 + a_p^2 + 2a_m a_p \sin(\Delta\phi)$ and $a_m^2 + a_p^2 - 2a_m a_p \sin(\Delta\phi)$ (see Supplementary Note 7). The power variations at $\pm\delta$ sidebands, as a function of $\Delta\phi$, are shown in Fig. 2d.

Experimental results. First, we show that light is generated on the $|a\rangle \rightarrow |b\rangle$ transition. The $\chi^{(2)}$ interaction mediated by these atoms between the pump and microwave fields results in a sum-frequency process that generates a corresponding signal optical field. By combining the generated optical light with an optical local oscillator, we detect the generated light at the heterodyne beat frequency $f_{het,S}$ (see Methods and Fig. 3a).

To probe the frequency-tunable nature of the conversion process, we scan the pump laser frequency across the Doppler width. At any instant during the scan, the pump field interacts with one velocity class of atoms, which see this frequency on resonance with the pump transition. The generated signal reaches a maximum amplitude between the $F = 2 \rightarrow F' = 1$ and $F' = 2$ transitions [Fig. 3b], with a full width at half maximum (FWHM) of 550(25) MHz. This generated spectrum corresponds to the combined Doppler-dependent absorption coefficients for the $F = 1 \rightarrow F' = 1, 2$ transitions, which has a FWHM of 540 MHz. The $F' = 3$ state does not participate in this nonlinear process, since selection rules prohibit an electric-dipole transition to the $F = 1$ ground state. Similarly, the pump transition from $F = 2 \rightarrow F' = 0$ is electric-dipole forbidden. We also characterize the effects of various pump and idler powers as shown in Fig. 3c, d. For a good signal-to-noise ratio, we typically operated with a pump power near 76 μW and idler power of 3.2 mW.

Next, we explore the multi-channel character of the conversion process. The pump laser is tuned halfway between the $F = 2 \rightarrow F' = 2$ & 3 transitions. By modulating either the idler or the pump, multiple frequency components are generated in the signal: First, we amplitude-modulate (AM) the microwave idler signal at ω_{AM} and observe sidebands in the signal at $\omega_S \pm \omega_{AM}$. The conversion bandwidth from idler modulation is limited to a maximum of 1 MHz by the width of the cavity resonance. Next, we additionally phase-modulate (PM) the pump using a fiber EOM in the optical path and observe that the idler and pump combine together as dictated by the sum-frequency process [Eq. (1)]. The MB width and density determine the bandwidth and amplitudes of the pump-modulated generated sidebands. Both types of sideband generation are illustrated in Fig. 4a, including simultaneous idler AM and pump PM. In the three cases depicted, $\omega_{AM}/2\pi = 50$ kHz is fixed and $\omega_{PM}/2\pi$ is varied from 10 MHz to 100 MHz.

When the pump and idler are modulated at the same frequency, $\omega_{PM} = \omega_{AM}$, the sidebands from each input overlap and interfere [Fig. 4b-i]. By tuning the relative phase of the modulating waves, one sideband or the other can be selectively enhanced or eliminated, with a relative visibility of 97% [Fig. 4b-ii], in qualitative agreement with the calculated variation shown in Fig. 2d.

The efficiency of conversion from microwave to signal photons is defined as the rate of signal photon production to the rate of
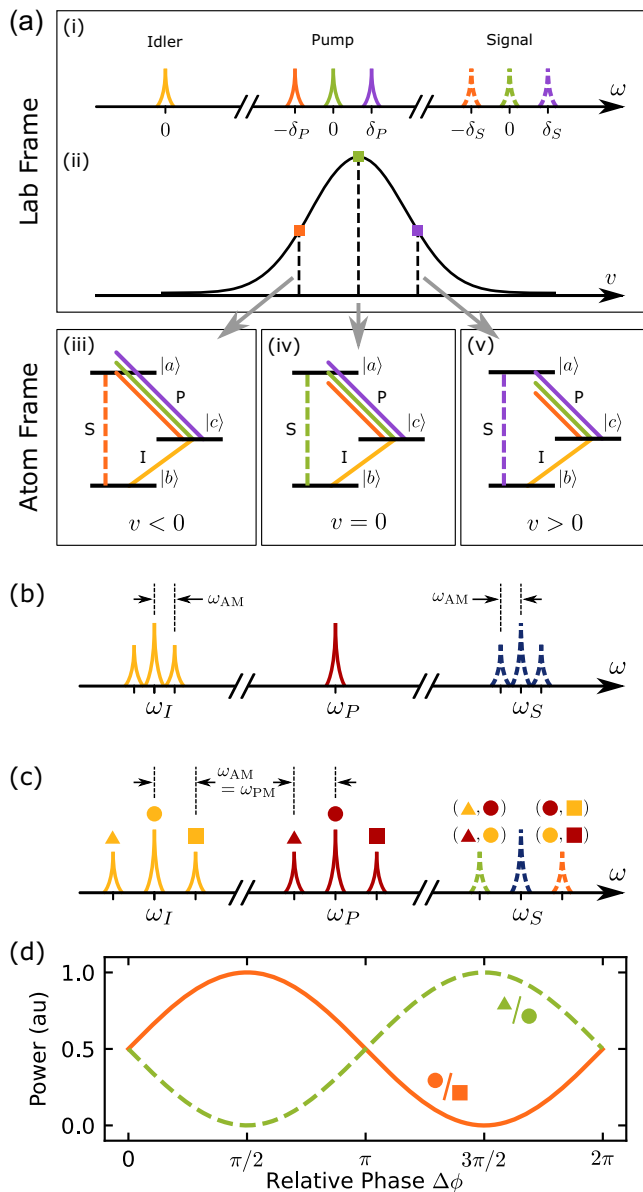
Fig. 2 Numerical simulations. a i Lab-frame cartoon depicting multiple pump frequency channels (central-green, upper-purple, lower-orange) combining with a single idler (yellow) to produce multiple signal channels. **a** ii These pump frequencies access independent atomic velocity classes from a thermal MB distribution. (a-iii to a-v) In their reference frame, atoms in these velocity classes see the respective pump frequency Doppler-shifted to resonance. Generation occurs in the velocity class for which the three-photon resonance condition (i.e. energy conservation) is satisfied. **b** Calculated spectra of an amplitude-modulated idler field showing sidebands (SBs); the carrier and SBs combine with the pump to produce a multichannel signal spectrum. **c** When the idler and pump are both modulated at the same frequency, multiple generation pathways interfere producing an upper and lower generated signal SBs. The input fields each have lower (▲), central (●), and upper (■) spectral peaks. **d** Calculated curves showing correlated signal SB amplitudes, which vary coherently with the relative phase of the two modulations depicted in (**c**). Both AM and PM modulation indices are 0.2.

microwave photons residing in the cavity mode[9,10]

$$\eta \equiv \frac{P_{\text{signal}}/\hbar\omega_{\text{signal}}}{P_{\text{idler}}/\hbar\omega_{\text{idler}}}. \qquad (5)$$

Further details on this calculation are included in Supplementary Notes 2, 3 and 6. We determine a maximum conversion efficiency of $\eta_0 = 1.5(1) \times 10^{-9}$. Efficiency in our system is primarily limited by a very low optical depth of 0.05(1). In comparison, cold atom conversion experiments have employed optical depths of up to 15[9] and 120[11]. Our optical depth corresponds to a number density of about 4×10^{16} cm^{-3} with $8.7(1) \times 10^8$ atoms in the interaction region. This atom number is ~10^9 times lower than the $3.2(1) \times 10^{18}$ available microwave photons in the same volume. At room temperature, the thermal noise is at the level of 900 photons, which is indiscernible compared to the signals used here. We note that it is this noise, determined by the temperature of the microwave electronics and transmission components (rather than of the conversion medium), that sets the limit of low-photon-number operation. Moving toward true quantum transduction requires reducing the noise in these components by operating at cryogenic temperatures[22].

Discussion

The frequency tunability of the generated signal field results from the existence of a large Doppler width at room temperature. While this work uses a warm vapor cell of enriched ^{87}Rb without an anti-relaxation coating or a buffer gas, a buffer gas would provide additional tunability due to collisional broadening[23–25]. This tunability is ultimately limited to the order of the ground-state hyperfine splitting of the atoms used.

While other conversion schemes display degrees of tunability of the output frequency[9,11,14,15], these are often restricted by natural atomic or optical cavity resonance frequencies. In the warm-atom system, a continuous tunability over the entire Doppler width is possible. This frequency multiplexing capability enables multiple microwave sources to be interfaced with a single atomic transducer, and the conversion can be used to place differing sources in distinct optical frequency domains. Switching between different optical frequencies for a single source is also possible. Our scheme features a conversion bandwidth of 910(20) kHz [see Fig. 6b], which is primarily limited by the cavity linewidth. As previously demonstrated in a different context[26], the reverse optical-to-microwave conversion process is achievable in an atomic three-wave mixing system.

The high-contrast amplitude control of signal sidebands enabled by simultaneous pump and idler modulation [Fig. 4b] is equivalent to a tunable beam-splitter operating in the frequency domain[16]. The modulation indices and the relative phase act together as reflection and transmission coefficients. For particular values of these coefficients we can selectively generate a chosen sideband channel in the optical domain while completely suppressing the other, resulting in single-sideband conversion.

Thus, our neutral atom system is capable of performing as a "quantum frequency processor"[17,27,28] with particularly low input-field intensities. This allows us not only to encode and manipulate information in multiplexed frequency bins but also to convert it from microwave to optical frequency domains.

The measured conversion efficiency is comparable with magnon-based microwave-to-optical conversion schemes[14,15]. The warm-atom efficiency is inherently limited by the intrinsic weakness of the magnetic-dipole microwave transition, as well as the ground-state spin decoherence γ_I which includes wall-collisions, transit-time decoherence, and Rb-Rb spin-exchange collisions (see Supplementary Note 5). A larger optical beam combined with a buffer gas[29,30] and anti-relaxation coating on the cell walls[31–34] would help reduce spin decoherence from the dark state and boost conversion efficiency. For example, we expect that a high-quality anti-relaxation coating and a modest 5 torr of neon would significantly reduce transit-time and wall effects, and
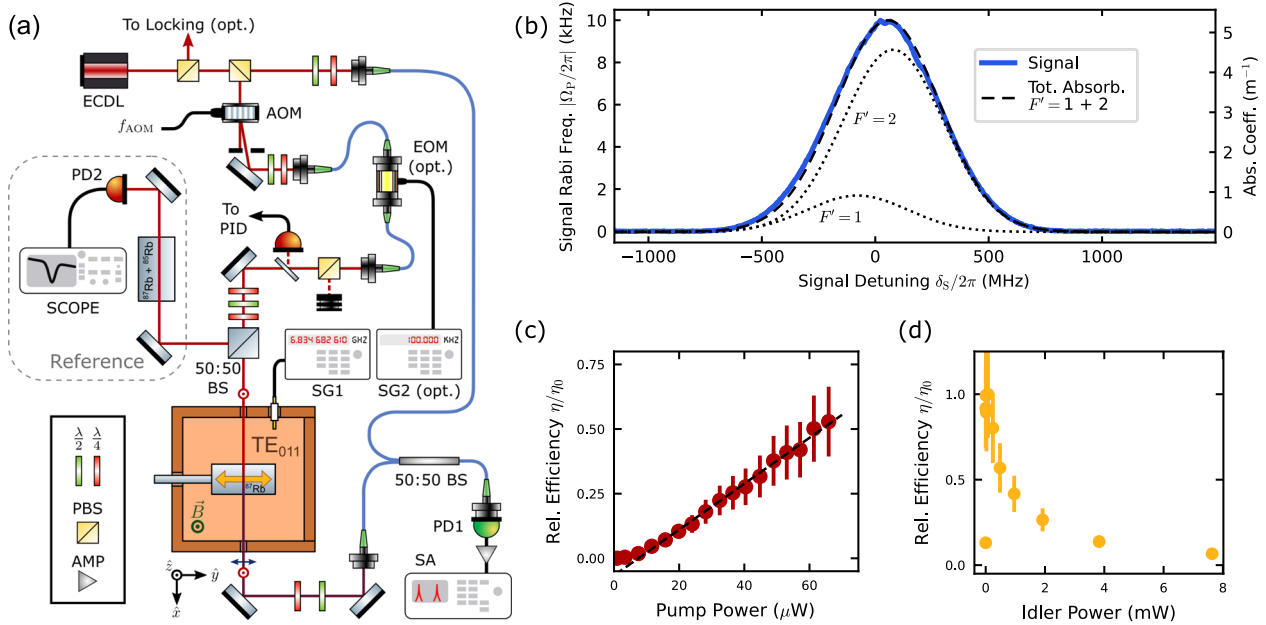
Fig. 3 Experimental setup and main results. a Schematic of the experimental setup: Central to the experiment is a microwave cavity supporting a TE_{011} mode, polarized along the y-axis. The light incident on the cavity is polarized along the z-axis and propagates along the x-axis. The vapor cell inside the cavity has enriched ^{87}Rb. Unshifted light from the external cavity diode laser (ECDL) is used as a local oscillator for heterodyne detection; it is combined with the other beam in a fiber 50:50 beam splitter (BS), producing two beat signals at $f_{het,P}$ and $f_{het,S}$. AOM - Acousto-optic modulator; EOM - Electro-optic modulator; SG - signal generator; SA - spectrum analyzer; PD - photodiode. **b** The generated signal measured with the spectrum analyzer in zero-span mode, showing a FWHM of 550(25) MHz. The dashed curve shows the calculated Doppler-broadened absorption coefficient of the pump light; the individual components due to the $F' = 1$ and $F' = 2$ excited hyperfine levels are shown as dotted curves. Without any fitting or free parameters, the generated signal data is proportional to the MB absorption distribution of the pump transitions. **c** The generated signal amplitude responds roughly linearly to increased pump optical power. **d** The response of the generated signal amplitude to microwave powers from SG1. The largest pump and idler powers measured correspond to intensities of about 3 & 7 mW/cm². Error bars represent the standard deviation.
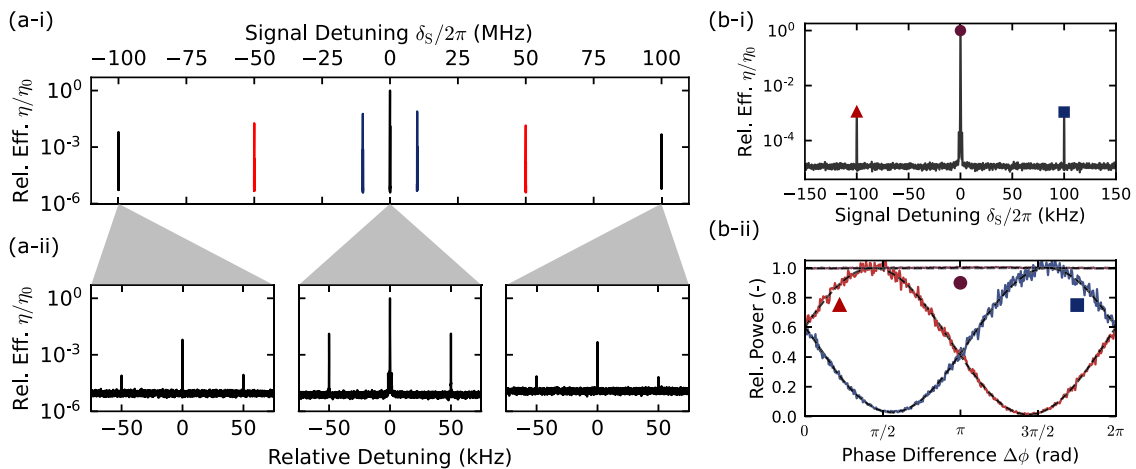

Fig. 4 Sideband generation and interference. a–i Multichannel generation using a fixed microwave amplitude modulation frequency of $\omega_{AM}/2\pi = 50$ kHz and a variable pump phase modulation frequency $\omega_{PM}/2\pi$ of 10 (blue), 50 (red) and 100 (black) MHz. The relative sideband amplitude decreases for increased ω_{PM} because the pump light accesses velocity classes with decreased occupation. **a**–ii Zoomed-in data revealing AM sidebands flanking each of the central and SB PM peaks. **b** When the two modulation frequencies are equal, i.e. $\omega_{PM} = \omega_{AM}$, the PM and AM sidebands overlap and interfere. The relative phase difference $\Delta\phi$ between the modulating waves controls the height of the correlated upper (■, blue) and lower (▲, red) generated sidebands. (b-i) The generated spectrum at zero relative phase. **b**–ii The relative power amplitude response of the peaks have a visibility of 97%, while the central peak (●, purple) is independent of the relative phase. The two SB amplitudes differ from each other by $(\pi - 0.38)$ radians of phase. The dashed lines show independent fits to a cosine.

reduce $\gamma_I/2\pi$ by a factor of 10^3 to 100 Hz, limited by Rb-Rb spin-exchange. Everything else being equal, this would provide a 10^6-fold improvement to the generation efficiency. Furthermore, based on[10], we expect that increased pump powers will produce a

moderate 4-fold efficiency gain before the efficiency saturates due to absorption and incoherent scattering of the pump.

In this proof-of-concept demonstration, we have shown that inhomogeneous Doppler broadening in a warm vapor cell provides significant tunability of the output optical frequency in a

microwave-optical transduction, resulting in frequency division multiplexing. The inhomogeneous width also enables simultaneous frequency up-conversion of multi-channel microwave inputs. Amplitude control of up-converted optical channels demonstrates analogous frequency domain beam splitting action across five orders in frequency. The frequency division multiplexing capability combined with amplitude control can make neutral atoms as quantum processors for information encoded in frequency bin qubits.

Methods

Experimental setup. The experimental setup can be seen in Fig. 3a. The pump optical field is derived from an continuous-wave external cavity diode laser (MOGLabs CEL) operating at 780.24 nm. This laser is frequency-stabilized to the saturated absorption spectrum of a separate Rb reference vapor cell. We have the option to lock the laser frequency 80 MHz below the $F' = 2-3$ crossover transition with a locked linewidth of ~100 kHz. Alternatively, we can unlock and move the laser frequency off-resonance. The pump beam is then shifted upwards in frequency by $f_{AOM} = 76.60$ MHz with an acousto-optical modulator and transmitted to the cavity-vapor cell apparatus via optical fiber. After the optical fiber, the polarization is filtered with a polarizing beam splitter (PBS) and the power of the pump light is stabilized with a servo controller (NuFocus LB1005) to <1% fluctuations. The Rabi frequency of the pump laser $\Omega_P/2\pi$ has a value of 3.5 MHz[35] and it is linearly polarized along the z-axis.

Inside the cavity[18,19], the idler microwave field is polarized along the y-direction. Orthogonal Helmholtz coils null the external magnetic field along the x and y-axes and apply a weak DC magnetic field $\vec{B}_z$ along the z-axis. The magnetic field strength makes a striking impact on the conversion efficiency. As shown in Fig. 5a, conversion is strongly suppressed at zero magnetic field and reaches maxima at ~±200 mG. This behavior is well-described by a symmetric, generalized Fano lineshape[36] that has the simplified form

$$\eta(B_z) = \eta'_0 \left[\frac{2\gamma_B(B_z - B_0)}{\gamma_B^2 + (B_z - B_0)^2} \right]^2. \tag{6}$$

This points to the participation and interaction of multiple Zeeman levels in the generation process. At Zeeman degeneracy, generation pathways may destructively interfere. The value $\gamma_B \times \gamma_0 = 140$ kHz $\sim \gamma_I$, the ground state decoherence rate, where γ_0 is the ground state gyromagnetic ratio of ^{87}Rb[37]. Further discussion goes beyond the scope of this work and will be the topic of future investigation.

The generated signal light emerges from the cavity polarized along the y-axis, orthogonal to the pump[38]. Before recoupling to an optical fiber, a half-waveplate is manually adjusted to optimize the signals at $f_{het,P}$ and $f_{het,S}$ for each respective measurement. The light is then combined in a 50:50 fiber BS with local oscillator laser light that was not shifted by the acousto-optic modulator (AOM). The interference produces heterodyne beat notes at $f_{het,P} = f_{AOM}$ and $f_{het,S} = \omega_\mu/2\pi + f_{AOM} = 6.911282$ GHz. A high bandwidth amplified photodiode (PD1, EOT ET-4000AF) detects the beating signals. This electronic signal is amplified (AMP, Mini-Circuits ZJL-7G+) and its amplitude is measured by a spectrum analyzer (SA, R&S FSV3013). This heterodyne peak at $f_{het,S}$ has a FWHM of 26(2) Hz [see Fig. 5b], larger than the <2 Hz linewidth of our microwave source, SG1. We presume the presence of additional perturbations (e.g. 60 Hz line noise) broadens and modulates our generated signal.
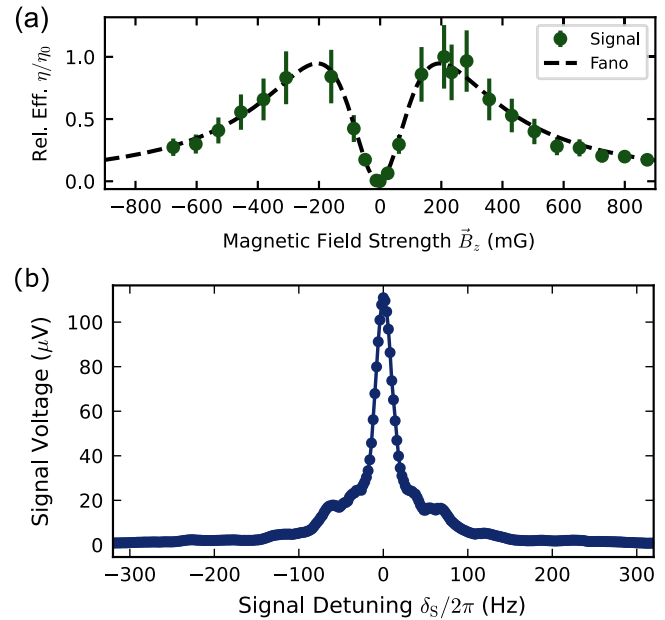

Fig. 5 Magnetic field effect and generated linewidth. a The generated signal's response to a variable magnetic field strength $\vec{B}_z$ along the z-axis. Wte operate at 209 mG for maximum generation. We fit a symmetric Fano profile [Eq. (6)] to these data, with fit parameters $\eta'_0 = 0.95(2)$, $\gamma_B = 200(4)$mG and $B_0 = -5(3)$mG. This behavior might indicate the interaction and interference of multiple Zeeman level resonances within the decoherence width of our atoms. Error bars represent the standard deviation. **b** A close up of the unmodulated generated line revealing a FWHM of 26(2) Hz.

Broad-tunability. To access all the frequencies within the Doppler profile, the pump frequency is scanned across the Doppler profile with a laser frequency sweep. We trigger the SA off the sweep ramp and measure the heterodyne signal in zero-span mode with a resolution bandwidth of 2 kHz. Simultaneous to the sweep, we also trigger and record the transmission of pump light through a reference vapor cell of rubidium (natural abundance) placed near the microwave cavity and at ambient 21.6(3) °C. We find good agreement between the measured spectrum and a theoretical transmission model[39]. Using the ^{87}Rb and ^{85}Rb transmission dip extrema, we calibrate our sweep rate to 17.2 MHz/ms and convert the time axis of the series to frequency [Fig. 6a].

Multichannel conversion. We generate a multichannel optical signal field in two different ways: first, the signal generator (SG1) supplying the idler field is amplitude-modulated at a variable ω_{AM}. We note that due the finite microwave cavity resonance (see Supplementary Note 1), $\omega_{AM}/2\pi$ can be tuned up to 455(10) kHz before the sidebands become significantly suppressed. Second, we modulate the pump light by using a fiber phase-modulator EOM (EOSPACE PM-0S5-20-PFA-PFA-780) inserted into the pump light optical path. We drive the EOM with a second signal generator (SG2, SRS SG384) at a variable ω_{PM}. This produces sidebands in the pump optical spectrum, and corresponding sidebands are visible in the generated spectrum around the heterodyne frequency $f_{het,S}$. The SA and SG2 are both phase-locked to the internal 10 MHz clock reference of SG1. In this second case, ω_{PM} can be tuned over the Doppler FWHM before the sidebands become significantly suppressed.
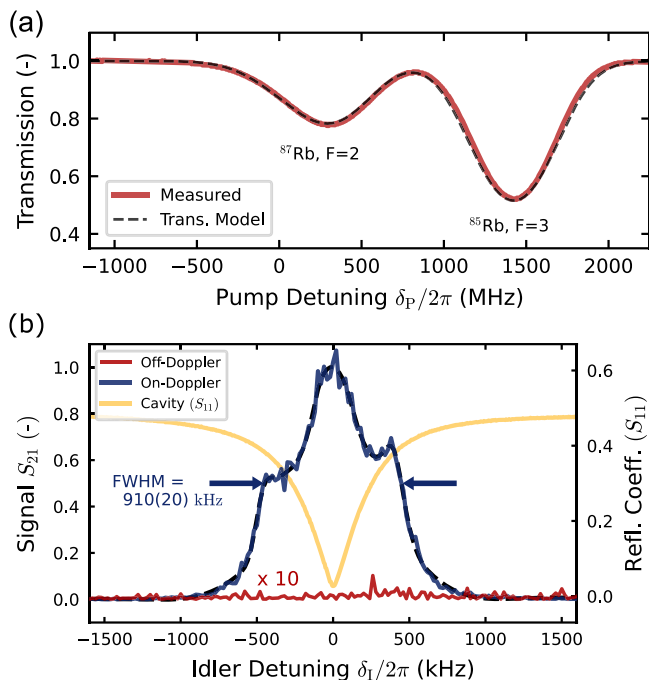
Fig. 6 Frequency sweep and conversion bandwidth. a The Doppler-broadened transmission spectrum of a reference rubidium vapor cell (outside the microwave cavity) at room temperature, measured while sweeping the pump laser frequency. The dotted line shows a transmission model curve with good agreement to the measured trace. This trace was taken simultaneous to the data shown in Fig. 3b; the positions of the two Doppler peaks are used to calibrate the horizontal frequency scale. **b** The raw generated signal during a scan of δ_I, as measured with a vector network analyzer (VNA) in S21 mode. We measure a conversion bandwidth (FWHM) of 910(20) kHz when the laser is locked on-resonance and with a z-magnetic field of 209 mG. The dashed line is a smoothing spline used to determine the bandwidth. No generation is visible when the laser is off-resonance. The cavity resonance has a FWHM of 417 kHz, as measured with the VNA in S11 mode.

Conversion bandwidth. We characterize the conversion bandwidth of our microwave-to-optical conversion process. To do this, we replace SG1 and SA with Ports 1 and 2, respectively of a VNA (Keysight E5063A). The generated signal is measured on the VNA in S21 mode and is shown in Fig. 6b. When the laser is locked on resonance and at the optimal magnetic field of 209 mG, a clear peak in the S21 signal is visible with FWHM = 910(20) kHz. This width is compared to the 417 kHz width of the cavity resonance. When the laser is off-resonance, no generation is apparent.

Data availability

References

1. Arute, F. et al. Quantum supremacy using a programmable superconducting processor. *Nature* **574**, 505–510 (2019).
2. Son, N. T. et al. Developing silicon carbide for quantum spintronics. *Appl. Phys. Lett.* **116**, 190501 (2020).
3. Storz, S. et al. Loophole-free Bell inequality violation with superconducting circuits. *Nature* **617**, 265–270 (2023).
4. Lambert, N. J., Rueda, A., Sedlmeir, F. & Schwefel, H. G. L. Coherent conversion between microwave and optical photons-an overview of physical implementations. *Adv. Quant. Technol.* **3**, 1900077 (2020).
5. Lauk, N. et al. Perspectives on quantum transduction. *Quant. Sci. Technol.* **5**, 020501 (2020).
6. Fan, L. et al. Superconducting cavity electro-optics: a platform for coherent photon conversion between superconducting and photonic circuits. *Sci. Adv.* **4**, eaar4994 (2018).
7. Hisatomi, R. et al. Bidirectional conversion between microwave and light via ferromagnetic magnons. *Phys. Rev. B* **93**, 174427 (2016).
8. Higginbotham, A. P. et al. Harnessing electro-optic correlations in an efficient mechanical converter. *Nat. Phys.* **14**, 1038–1042 (2018).
9. Han, J. et al. Coherent microwave-to-optical conversion via six-wave mixing in Rydberg atoms. *Phys. Rev. Lett.* **120**, 093201 (2018).
10. Adwaith, K. V., Karigowda, A., Manwatkar, C., Bretenaker, F. & Narayanan, A. Coherent microwave-to-optical conversion by three-wave mixing in a room temperature atomic system. *Opt. Lett.* **44**, 33 (2019).
11. Tu, H.-T. et al. High-efficiency coherent microwave-to-optics conversion via off-resonant scattering. *Nat. Photon.* **16**, 291–296 (2022).
12. Borówka, S., Pylypenko, U., Mazelanik, M. & Parniak, M. Continuous wideband microwave-to-optical converter based on room-temperature Rydberg atoms. *Nat. Photon.* https://doi.org/10.1038/s41566-023-01295 (2023).
13. Vogt, T. et al. Efficient microwave-to-optical conversion using Rydberg atoms. *Phys. Rev. A* **99**, 023832 (2019).
14. Zhu, N. et al. Waveguide cavity optomagnonics for microwave-to-optics conversion. *Optica* **7**, 1291–1297 (2020).
15. Shen, Z. et al. Coherent coupling between phonons, magnons, and photons. *Phys. Rev. Lett.* **129**, 243601 (2022).
16. Lu, H. H. et al. Electro-optic frequency beam splitters and tritters for high-fidelity photonic quantum information processing. *Phys. Rev. Lett.* **120**, 30502 (2018).
17. Lukens, J. M. Quantum information processing with frequency-bin qubits: progress, status, and challenges. In *Conference on Lasers and Electro-Optics* (OSA, 2019).
18. A. Tretiakov, C. A. Potts, T. S. Lee, M. J. Thiessen, J. P. Davis, L. J. LeBlanc. Atomic microwave-to-optical signal transduction via magnetic-field coupling in a resonant microwave cavity. *Appl. Phys. Lett.* **116**, 164101 (2020).
19. M. Ruether, C.A. Potts, J.P. Davis and L.J. LeBlanc. Polymer-loaded three dimensional microwave cavities for hybrid quantum systems. *J. Phys. Commun.* **5** 121001 (2021).
20. Adwaith, K. V. et al. Microwave controlled ground state coherence in an atom-based optical amplifier. *OSA Contin.* **4**, 702 (2021).
21. Lu, H.-H. et al. Quantum interference and correlation control of frequency-bin qubits. *Optica* **5**, 1455 (2018).
22. Kumar, A. et al. Quantum-limited millimeter wave to optical transduction. *arXiv* http://arxiv.org/abs/2207.10121 (2022).
23. Peng, J., Liu, Z., Yin, K., Zou, S. & Yuan, H. Determination of the partial and total pressures of the mixed gases in atomic vapor cells by optical absorption. *J. Phys. D Appl. Phys.* **55**, 365005 (2022).
24. Zameroski, N. D., Hager, G. D., Rudolph, W., Erickson, C. J. & Hostutler, D. A. Pressure broadening and collisional shift of the Rb D2 absorption line by CH4, C2H6, C3H8, n-C4H10, and He. *J. Quant. Spectr. Radiat. Trans.* **112**, 59–67 (2011).
25. Ha, L.-C., Zhang, X., Dao, N. & Overstreet, K. R. D1 line broadening and hyperfine frequency shift coefficients for ^{87}Rb and ^{133}Cs in Ne, Ar, and N2. *Phys. Rev. A* **103**, 022826 (2021).
26. Godone, A., Levi, F. & Vanier, J. Coherent microwave emission in cesium under coherent population trapping. *Phys. Rev. A* **59**, R12 (1999).
27. Lukens, J. M. & Lougovski, P. Frequency-encoded photonic qubits for scalable quantum information processing. *Optica* **4**, 8 (2017).
28. Olislager, L. et al. Frequency-bin entangled photons. *Phys. Rev. A* **82**, 1–7 (2010).
29. Franzen, W. Spin relaxation of optically aligned rubidium vapor. *Phys. Rev.* **115**, 850–856 (1959).
30. Finkelstein, R., Bali, S., Firstenberg, O. & Novikova, I. A practical guide to electromagnetically induced transparency in atomic vapor. *J. Phys.* **25**, 035001 (2023).
31. Li, W. et al. Characterization of high-temperature performance of cesium vapor cells with anti-relaxation coating. *J. Appl. Phys.* **121**, 063104 (2017).
32. Balabas, M. V., Karaulanov, T., Ledbetter, M. P. & Budker, D. Polarized alkali-metal vapor with minute-long transverse spin-relaxation time. *Phys. Rev. Lett.* **105**, 070801 (2010).
33. Chi, H., Quan, W., Zhang, J., Zhao, L. & Fang, J. Advances in anti-relaxation coatings of alkali-metal vapor cells. *Appl. Surf. Sci.* **501**, 143897 (2020).
34. Jiang, S. et al. Observation of prolonged coherence time of the collective spin wave of an atomic ensemble in a paraffin-coated ^{87}Rb vapor cell. *Phys. Rev. A* **80**, 062–303 (2009).

35. Šibalić, N., Pritchard, J., Adams, C. & Weatherill, K. Arc: An open-source library for calculating properties of alkali Rydberg atoms. *Comp. Phys. Commun.* **220**, 319–331 (2017).
36. Caselli, N. et al. Generalized Fano lineshapes reveal exceptional points in photonic molecules. *Nat. Commun.* **9**, 396 (2018).
37. Steck, D. A. *Rubidium 87 D Line Data.* https://steck.us/alkalidata/rubidium87numbers.1.6.pdf (2003).
38. Campbell, K. et al. Gradient field detection using interference of stimulated microwave optical sidebands. *Phys. Rev. Lett.* **128**, 163602 (2022).
39. Siddons, P., Adams, C. S., Ge, C. & Hughes, I. G. Absolute absorption on rubidium D lines: comparison between theory and experiment. *J. Phys. B Atom. Mol. Opt. Phys.* **41**, 155004 (2008).

Acknowledgements

Author contributions

B.D.S. and A.N. developed the concept for the experiment, and A.N. provided the models used. Experiments were performed by B.D.S., B.B., and A.N. and analyzed by BDS with input from A.N. The manuscript was initially prepared by B.D.S. and A.N., and all authors contributed to review and editing. L.J.L. supervised the project.

Competing interests

The authors declare no competing interests.

Additional information

Supplementary information The online version contains supplementary material available at https://doi.org/10.1038/s42005-023-01455-y.

Correspondence and requests for materials should be addressed to Benjamin D. Smith or Lindsay J. LeBlanc.

Peer review information *Communications Physics* thanks the anonymous reviewers for their contribution to the peer review of this work. A peer review file is available.

Reprints and permission information is available at http://www.nature.com/reprints

Publisher's note Springer Nature remains neutral with regard to jurisdictional claims in published maps and institutional affiliations.